



Influence of anodization conditions on deposition of hydroxyapatite on α/β Ti alloys for osseointegration: Atomic force microscopy analysis

Rania E. HAMMAM¹, Engie M. SAFWAT², Soha A. ABDEL-GAWAD³, Madiha SHOEIB⁴, Shima EL-HADAD⁴

1. Faculty of Engineering, Modern University for Technology and Information (MTI), Cairo 11585, Egypt;

2. Restorative and Dental Materials Department, National Research Centre, Giza 12622, Egypt;

3. Chemistry Department, Faculty of Science, Cairo University, Giza 12613, Egypt;

4. Central Metallurgical Research and Development Institute, CMRDI, P.O. 87, Helwan 11421, Egypt

Received 10 June 2023; accepted 4 January 2024

Abstract: Integrating titanium-based implants with the surrounding bone tissue remains challenging. This study aims to explore the impact of different anodization voltages (20–80 V) on the surface topography of two-phase (α/β) Ti alloys and to produce TiO₂ films with enhanced bone formation abilities. Scanning electron microscopy coupled with energy dispersive spectroscopy (SEM-EDS) and atomic force microscopy (AFM) were applied to investigate the morphological, chemical, and surface topography of the prepared alloys and to confirm the growth of hydroxyapatite (HA) on their surfaces. Results disclosed that the surface roughness of TiO₂ films formed on Ti-6Al-7Nb alloys was superior to that of Ti-6Al-4V alloys. Ti-6Al-7Nb alloy anodized at 80 V had the highest yields of HA after immersion in simulated body fluid with enhanced HA surface coverage. The developed HA layer had a mean thickness of (128.38±18.13) μ m, suggesting its potential use as an orthopedic implantable material due to its promising bone integration and, hence, remarkable stability inside the human body.

Key words: material science; electrochemical anodization process; atomic force microscopy; α/β Ti alloys; hydroxyapatite deposition

1 Introduction

The commercial two-phase (α/β type) Ti-6Al-4V alloy has been extensively utilized as an orthopedic biomaterial for structural support owing to its excellent specific strength and biocompatible characteristics. Nevertheless, it was stated that the liberation of vanadium ions during the operation of the alloy might cause health problems due to their toxicity [1].

Recently, Ti-6Al-7Nb alloy is part of a new generation of materials that can be utilized as orthopedic implants. Ti-6Al-7Nb alloy has both α and β phases, where niobium replaces vanadium of Ti-6Al-4V alloy, stabilizing β phase.

In comparison to Ti-6Al-4V alloy, Ti-6Al-7Nb alloy possesses higher corrosion resisting ability and can be easily fabricated into components having complex contours due to its higher ductility [2]. Several in vitro and in vivo studies inspected the biocompatibility of aluminum-enclosing titanium alloys, and they found that the biocompatibility of these alloys depends mainly on the chemical composition of the surface of the alloy rather than their bulk composition [3]. Additionally, the high corrosion resistance of titanium alloys owing to their surface TiO₂ layer renders them non-susceptible to release of Al ions into the body [4]. It is worth mentioning that Ti-6Al-7Nb alloy was reported to fulfill the requirements of the ISO 5832-11 standard [5]. In a study presented by

EL-HADAD et al [6], functionally graded Ti–6Al–7Nb and Ti–6Al–4V alloys revealed high cytocompatibility and in vivo systemic safety in experimental animals.

Though the central focus of this study is on Ti–6Al–4V and Ti–6Al–7Nb alloys, other titanium alloys have been investigated previously for orthopedic purposes, including binary alloys Ti–Zr [7] and Ti–Nb [8], ternary alloys (Ti–13Nb–13Zr) [9], and quaternary alloys (Ti–Nb–Ta–Zr and Ti–Nb–Zr–Fe) [10], where oxide nanotubes have been successfully prepared on the surface of these alloys.

The inert nature and lack of bone–titanium osseointegration remain a big challenge, as they affect the implant stability and delay bone healing. Hence, numerous efforts were conducted through engineering the surface characteristics of Ti alloys to improve the biocompatibility and fatigue life of the implant and to enhance bonding with the host bone tissue. Various techniques for the surface modification have been investigated to adapt the physical and chemical qualities of Ti alloys, including sand blasting [11], plasma spraying [12], sol–gel [13], ceramic coatings (SiC or hydroxyapatite) [14], chemical vapor deposition [15] and anodic oxidation [16,17]. Among these techniques, anodization has gained particular consideration owing to its exceptional assets such as its simple method, cost-effectiveness [18] and utility in producing nanophase coatings with enhanced corrosion resistance, adhesion and interfacial bonding with easily adjustable characteristics [19].

Electrochemical anodization is an electrolytic process employed to expand, the naturally occurring, oxide film thickness on metal surfaces [20] and to produce micro- or nano-porous TiO₂ coatings, having elevated roughness and surface energies [21]. However, the development of the oxide layer on the alloy surface is insufficient to evaluate the capability of material to integrate to the surrounding bone. It was suggested that the deposition of apatite on the surface of a biomaterial in simulated body fluid (SBF) can predict its bioactivity and osseointegration properties [22].

Hydroxyapatite (HA, Ca₁₀(PO₄)₆(OH)₂) is the main inorganic component of bone with approximately 69 wt.% [23]. From a biological perspective, the deposition of HA coatings on the implant surface is highly desirable since HA is a

very stable form of calcium phosphate and is the natural composition of bone [24,25]. STEPIEŃ et al [26] explored the electrochemical synthesis of oxide nanotubes on the surface of Ti–6Al–7Nb alloys and their effect on apatite precipitation in SBF. They concluded that the apatite deposited only on alloy samples after anodization and that a potential of 30 V was adequate for precipitation of the oxide nanotubes suitable for biological integration. CHERNOZEM et al [27] studied the RF-magnetron sputtering of the HA coating on the surface of TiO₂ nanotubes synthesized at 30 and 60 V, respectively. The results showed that HA coating entirely covered the tubular surfaces of the nanotubes when a voltage of 30 V was applied. However, a homogeneous CaP coating was not visible at 60 V.

Recently, atomic force microscopy (AFM) has been introduced as a modern valuable tool for investigation of the surface topography of thin films [28]. It provides measurable data on the surface structures and physical qualities in extremely fine details [29]. The morphological information such as roughness and maximal and mean heights of thin films structures can be computed through AFM imaging [30].

Electrochemical anodization was employed in this work to modify the surface of Ti–6Al–7Nb and Ti–6Al–4V alloys to enhance their bone-bonding strength, and the effects of various anodization voltages on the surface topography and roughness of these alloys were explored. To assess the bone-bonding abilities of the anodized Ti alloys, the immersion in SBF was investigated since it is an economic and cost-effective procedure. The capability of the TiO₂ coatings to promote HA formation or growth was studied based on the quantity of HA that deposits or adheres to the surface of the alloys and overall HA surface coverage. Scanning electron microscopy along with energy dispersive spectroscopy (SEM–EDS) and AFM were applied to evaluate the morphological, chemical, and surface topography of the tested samples and to confirm the existence of HA on the surfaces of the Ti alloys.

2 Experimental

2.1 Fabrication of forged Ti alloy specimens

Ti–6Al–7Nb and Ti–6Al–4V forged alloy

samples were received as 10 and 8 mm diameter bars, respectively from Baoji Xuhe Titanium Metal Co., Ltd. The bars were processed by melting in a 500 kg vacuum induction furnace, and then they were forged and machined [31,32]. The alloying element compositions of the bars are presented in Table 1.

2.2 Sample preparation

Ten samples of Ti alloy discs (five Ti–6Al–7Nb and five Ti–6Al–4V alloys) were embedded in an epoxy resin block, exposing an area of 0.5 cm². A stainless-steel rod coated with Teflon held each disc to attain complete confinement when submerged in the electrolyte solution. The discs were ground on both sides with silicon carbide paper up to 2400 grit, and then they were mechanically polished with alumina pastes of 1 µm. The polished samples were ultrasonically washed in deionized water for 5 min, and then etched in a mixture of 80 mL/L HNO₃, 60 mL/L HF, and 150 mL/L H₂O₂ for 5 min at room temperature. Next, they were ultrasonically cleaned in deionized water for 5 min followed by air drying. Acid etching was utilized to obtain rougher surfaces with a better-adhering ability to the oxide layers and to produce adequate and uniform surface finishes.

2.3 Electrochemical anodization

2.3.1 Anodization principle

The anodization process is an in-situ electrochemical method for precipitating a tailored oxide layer on the anode surface of a metal substrate by employing an electrical field to aid the ionization of components in the aqueous electrolyte and their migration to the metal [4]. Anodizing of titanium alloys can be categorized into three main categories according to the properties of the generated oxides: conventional anodizing (interference-colored thin compact films), anodizing in electrolytes containing fluorides (nanotubular oxides), and plasma electrolytic oxidation (PEO) or micro-arc oxidation (MAO) at high voltages [33].

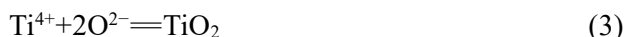
The oxide film growth is induced by a balance between the electrochemical generation of the oxide film and its dissolution due to chemical interaction with the components of the electrolyte. It was previously mentioned that the formation rate of anodic oxide greatly surpasses the dissolution rate in acid electrolytes such as sulfuric acid, oxalic acid, acetic acid, or phosphoric acid [34,35]. The product processing in such solutions leads to the formation of interference-colored oxide films on titanium.

The multi-beam interference theory can justify the color of anodized titanium [36]. As stated by the theory, interference colors are influenced by the non-regularity of the oxide layers on the titanium substrate. Interference colors can be produced by beams reflected from the oxide surface and the interface between surface oxide and titanium substrate. The color of the oxide layer will vary according to the increase in oxide thickness. Additionally, the variation in crystal structures of the anodic layers can also cause a color difference in the oxide layer [34].

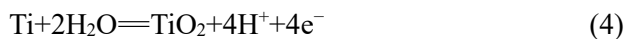
The anodization mechanism of titanium alloys in oxalic acid is explained as follows [37,38]: Once the voltage is applied to the anode of an electrochemical cell, which is the titanium alloy, an oxidation reaction will begin at the metal/TiO₂ interface (Reaction (1)) and Ti⁴⁺ ions are generated. Under the applied voltage, these Ti⁴⁺ ions diffuse outwards, while O²⁻ ions stemming from deprotonation of H₂O (Reaction (2)) existing in the electrolyte migrate toward the substrate/oxide interface. Along the movement of negatively charged O²⁻ ions toward the substrate/TiO₂ interface, they come across Ti⁴⁺ ions evolved from the surface and form a compact titanium oxide film (Reaction (3)). This field-assisted ion migration results in the growth of the oxide film at both interfaces, according to Reaction (3). The oxide layer will continue to thicken during anodization if the electric field is strong enough to provoke ionic conduction across the oxide.

Table 1 Alloying element compositions of Ti–6Al–4V and Ti–6Al–7Nb alloys (wt.%)

| Alloy | Al | Nb | V | Ta | Fe | C | O | N | Others | Ti |
|------------|-----|------|------|-------|------|-------|------|-------|--------|------|
| Ti–6Al–7Nb | 6.2 | 6.8 | 0.01 | <0.05 | 0.03 | <0.01 | 0.14 | <0.01 | <0.4 | Bal. |
| Ti–6Al–4V | 6.1 | 0.01 | 4 | 0 | 0.1 | 0.02 | 0.03 | 0.01 | <0.4 | Bal. |



The overall reaction is shown in Reaction (4):



2.3.2 Electrochemical anodization process

The polished Ti–6Al–7Nb and Ti–6Al–4V alloy discs were anodized under different conditions by changing the direct current (DC) voltages at a constant current. Ti oxide films were generated in a 10 wt.% aqueous oxalic acid dihydrate solution by applying different voltages (20, 40, 60 and 80 V) for 30 s at room temperature. The galvanostatic electrolysis was performed, with the cell voltage set to a value between 20 and 80 V using a DC power supply. The designed electrochemical cell consisted of two electrodes: the working electrode (anode) was made from Ti alloy discs, and the cathode was made of a platinum basket. A distance of 4 cm separated the cathode and anode.

2.4 Deposition of HA

Ti–6Al–7Nb and Ti–6Al–4V alloys anodized at different DC voltages were summarized in Table 2. Ti alloy samples were then subjected to static immersion [39], where they were separately incubated for 42 d in an incubator (Shaking incubator SI–100R HYSC, Korea) at 37 °C in 25 mL SBF. The SBF consisted of a mixture of sodium chloride, sodium hydrogen carbonate, potassium chloride, di-potassium hydrogen phosphate trihydrate,

magnesium chloride hexahydrate, calcium chloride, sodium sulfate, tris-hydroxymethyl aminomethane and hydrochloric. The pH was adjusted to 7.4, according to KOKUBO and TAKADAMA [22]. The pH values of the immersion solutions were recorded for each sample after 7, 14, 21, 28, 35, and 42 d of incubation using a pH meter (Jenway 3505, Bibby Scientific Limited, UK).

2.5 Surface characterization

To investigate the surface roughness and morphology of the tested Ti samples, AFM (Anton Paar-Tosca™ 200, USA) was utilized. 2D and 3D AFM images of the surface of the TiO₂ layers formed after the anodization of Ti alloys and after immersion in SBF for 42 d were recorded at randomly selected sites. A scanning size of 10 μm × 10 μm with a resolution of 400 × 400 was acquired using Arrow NCR tapping cantilever. The AFM data was treated according to ISO 25178 to evaluate the surface roughness using the Tosca analysis software specialized program. Profile graphs were obtained in sites where the distribution of peaks and pits was frequent and homogenous. To give a typical profile image for each sample, sites that represented the highest peaks and valleys were obtained using the software analysis of the entire examined 3D-viewed sample.

In addition, scanning electron microscope (SEM, JEOL-JSM–5410, Japan) coupled with an energy dispersive spectrometer unit (EDS-Oxford) was used to assess the surface morphologies of the alloys, elemental composition, and mapping, respectively.

To determine the thickness of the HA layers formed on the surface of anodized Ti alloys, a cross-section of selected samples was further prepared. Then, the samples were placed in bakelite and dried at room temperature. Next, the samples in the bakelite were ground using silicon carbide paper up to 2400 grit, and the thicknesses of the layers were analyzed by SEM.

2.6 Surface roughness parameters

The roughness parameters (S_a , S_q , S_{sk} , S_{ku}) in this study were based on the entire 3D surface, which provided more crucial values [40].

S_a is related to the arithmetical mean deviation of the roughness estimated over the calculated 3D surface:

Table 2 Anodization conditions of two-phase Ti alloy samples

| Sample No. | Alloy | Anodization voltage/V |
|------------|------------|-----------------------|
| 1 | Ti–6Al–7Nb | 0 |
| 2 | Ti–6Al–7Nb | 20 |
| 3 | Ti–6Al–7Nb | 40 |
| 4 | Ti–6Al–7Nb | 60 |
| 5 | Ti–6Al–7Nb | 80 |
| 6 | Ti–6Al–4V | 0 |
| 7 | Ti–6Al–4V | 20 |
| 8 | Ti–6Al–4V | 40 |
| 9 | Ti–6Al–4V | 60 |
| 10 | Ti–6Al–4V | 80 |

$$S_a = \iint_a |Z(x, y)| dx dy \quad (5)$$

where a is the defined area, and $Z(x, y)$ is the height/profile surface function.

S_q is related to the root mean square deviation of the roughness estimated over the calculated 3D surface:

$$S_q = \sqrt{\iint_a [Z(x, y)]^2 dx dy} \quad (6)$$

Surface skewness parameter S_{sk} of the 3D surface texture was computed to examine the symmetry of the distribution of the surface structures. A histogram of the heights of all measured points was performed, and the departure from normal distribution is represented by S_{sk} . Positive S_{sk} values mean that peaks dominate the surface, whereas negative values indicate valleys are more prominent.

$$S_{sk} = \frac{1}{S_q^3} \iint_a [Z(x, y)]^3 dx dy \quad (7)$$

To calculate the spikiness of height distribution of the 3D surface texture, coefficient of kurtosis (S_{ku}) was computed. A height distribution histogram for all measured points was established, and the deflection from normal distribution is denoted by S_{ku} :

$$S_{ku} = \frac{1}{S_q^4} \iint_a [Z(x, y)]^4 dx dy \quad (8)$$

If $S_{ku} < 3$, the surface is considered bumpy, if $S_{ku} = 3$, the surface has Gaussian distribution, and if $S_{ku} > 3$, the surface is spiky.


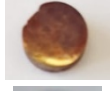








3 Results and discussion

3.1 Optical characteristics of TiO₂ films

Table 3 shows the photographic images of the untreated and anodized Ti alloy samples at different DC anodization voltages. The prepared Ti alloy discs without anodization appeared gray, having a metallic shine. After anodization, the discs retained a bright appearance but had different colors depending on the voltage applied, indicating the TiO₂ film formation on the surface of Ti–6Al–7Nb and Ti–6Al–4V samples. The observed colors of the surface of Ti alloy samples can be attributed to the interference phenomenon of reflected light between the interfaces of the oxide films (oxide surface and surface oxide/Ti substrate interface),

which was explained previously in Section 2.3.1. Moreover, because the surface topography of the titanium oxide layer that resembles rolling hills and valleys, when light rays fell on the anodized surface, reflection of light took place at different angles for each anodized specimen processed under different voltages. As a result, different scattered images were created, which displayed different colored surfaces for each oxide layer [41].

Table 3 Optical characteristics of oxide films at different applied cell voltages

| Sample No. | Alloy | DC voltage/V | Oxide film color | Image |
|------------|------------|--------------|------------------|---|
| 1 | Ti–6Al–7Nb | 0 | – |  |
| 2 | Ti–6Al–7Nb | 20 | Goldish orange |  |
| 3 | Ti–6Al–7Nb | 40 | Greenish blue |  |
| 4 | Ti–6Al–7Nb | 60 | Yellowish orange |  |
| 5 | Ti–6Al–7Nb | 80 | Dark yellow |  |
| 6 | Ti–6Al–4V | 0 | – |  |
| 7 | Ti–6Al–4V | 20 | Dark blue |  |
| 8 | Ti–6Al–4V | 40 | Light blue |  |
| 9 | Ti–6Al–4V | 60 | Goldish yellow |  |
| 10 | Ti–6Al–4V | 80 | Purple |  |

Ti alloy samples prepared with DC voltages greater than 80 V were not discussed in this study because applying higher potentials results in the electrical breakdown of the passive coatings, which is escorted by visible sparking and audible cracking [42].

SUL et al [34] concluded that the color of the Ti alloy surface changed according to the oxide thickness, which was influenced by the applied

voltage and type of electrolyte used. PILIPENKO et al [38] studied the impact of the electrolysis parameters on the electrochemical oxidation of VT6 Ti alloy in oxalic acid. Results revealed that the color of the oxide film changed according to the applied voltage (0–100 V). It was concluded that the color of the oxide film and the maximal thickness depended only on the cell voltage. BANDEIRA et al [43] anodically oxidized Ti–6Al–4V alloy in aqueous oxalic acid dihydrate solution to avoid the issue of fluoride toxicity. They found that different colored surfaces with estimated thicknesses in the range of 100–500 nm were obtained with the increase in applied AC voltages (10–80 V) and a slight effect on the roughness of the oxide layers was noted.

3.2 Surface topography of anodized Ti alloys

The surfaces of the Ti alloy discs were analyzed by AFM to determine the morphological parameters of the surfaces and to interpret the growth of the TiO₂ films according to the change in anodization voltage. Figure 1 shows the 2D and 3D AFM images of Ti–6Al–7Nb surfaces after anodization at different voltages. Obviously, the Ti alloy surfaces were greatly influenced by anodization. As shown in Fig. 1(a), the surface of the Ti–6Al–7Nb disc before anodization was covered with longitudinal, parallel grooves, probably due to grinding, which was also apparent when a 20 V was applied but with a somewhat homogeneous surface. The appearance of these fine grooves reveals the high precision and sub-nanometer resolution powers of the AFM tool, which showed even the finest details on the surface of the samples [44]. However, at higher anodic voltages, no apparent lines were visible due to the increase of anodic reactions and the formation of anodic films, masking any traces of grinding that could be present. With the increase of voltage up to 60 V, the surface became irregular with valleys and few distinct spikes. At 80 V, it was clear that the surface was entirely covered with an oxide layer and the surface was dominated by valleys and large hemispherical globular TiO₂ particles that were incorporated in the anodic films. There was also a possibility of formation of salts incorporated in this anodic film. These particles might have been created during the growth process of the oxide film. This implies that at higher DC voltages, there is increased growth of surface

structures with subsequent densification of large particles on the surface.

Figure 2 revealed that the surface textures of the anodized Ti–6Al–4V samples differed from those of anodized Ti–6Al–7Nb alloys. The surfaces of the anodized Ti–6Al–4V discs were covered with small-clustered structures and irregularities with protruding elevations and depressions, as shown in the 3D images. However, the 2D images revealed that the surfaces of the oxide films were nearly homogeneous for all anodized alloys. Valleys and distinct sharp peaks were distributed all over the surface of the Ti alloy substrates at different voltages (20–80 V) caused by the formation of cone-shaped oxide layers covering the surface area of the Ti alloy specimens. This same morphology was similar to a study by MALLAIAH and GUPTA [45], who modified surfaces of Ti64 by anodic oxidation at different voltages between 10 and 90 V in dilute sulfuric acid and plasma treatment to enhance the biocompatibility of Ti materials. They observed the same morphology of tiny clusters and irregularities with valleys and peaks of TiO₂ films. The surface roughness parameters of TiO₂ films formed on the surface of Ti alloys at different DC voltages are presented in Table 4.

It was clear from the surface roughness results shown in Table 4 that S_a of the Ti–6Al–7Nb alloy initially decreased from 123.0 nm without anodization to 40.4 nm at 40 V and then increased again to 185.7 nm at 60 V. The surface roughness then continued to increase with anodization voltage until it reached a value of 279.3 nm at 80 V.

The same phenomena were also observed for the Ti–6Al–4V alloy where S_a decreased from 187.7 nm without anodization to 97.8 nm at 20 V and then rose to 120.2 nm at 40 V and then proceeded to 204.2 nm at 80 V. It was clear that the roughness values of the Ti–6Al–7Nb alloys at anodization voltages of 60 and 80 V were higher than its counterpart alloys at the same applied voltages, which makes them more suitable for orthopedic applications since rough surfaces facilitate osseointegration of implants. Also high surface roughness enhances cells and tissues adhesion and thus improves implant stability into bone [46].

Moreover, the height differences in the 3D AFM images in Fig. 1 (Ti–6Al–7Nb surfaces) were much higher than those in Fig. 2 (Ti–6Al–4V

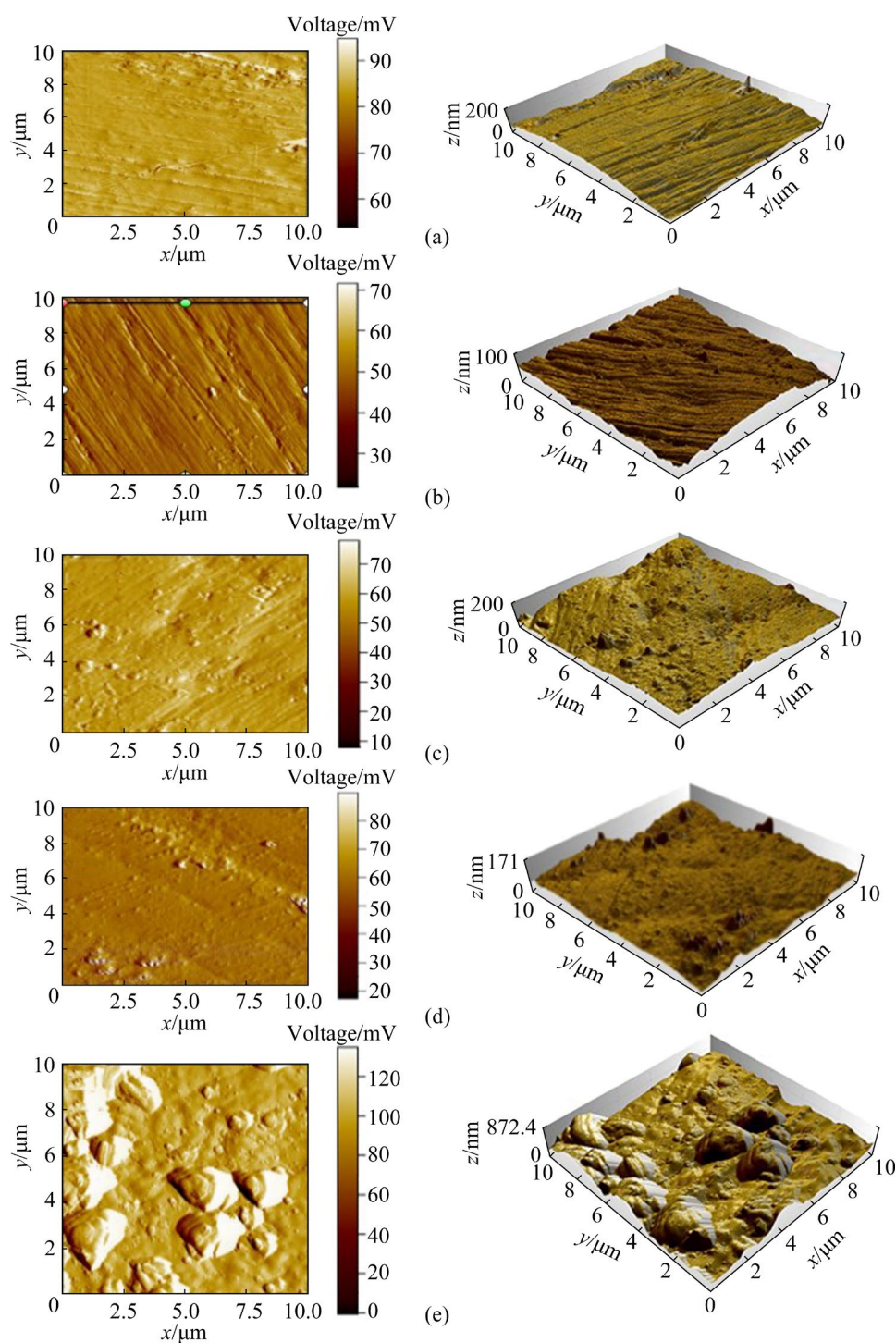


Fig. 1 2D and 3D AFM images of Ti-6Al-7Nb surfaces after anodization at different DC voltages: (a) Sample 1; (b) Sample 2; (c) Sample 3; (d) Sample 4; (e) Sample 5

surfaces), which confirmed the higher roughness features of the anodized Ti-6Al-7Nb alloys. The initial decrease of surface roughness for both types of alloys at low voltages can be attributed to the slow reactions and the development of a very thin TiO_2 oxide layer having a somewhat flattened structure, which consequently lowered the roughness of the films. However, with higher

voltages, the surface roughness increased again because higher voltages permitted higher electrical charges necessary for anodic film growth and, as a result, an increase in the titanium oxide films or grains grown onto the samples [47].

Furthermore, high voltages cause an increase in the inward transfer of O^{2-} into the metal-film interface along with the diffusion of Ti^{4+} ions from

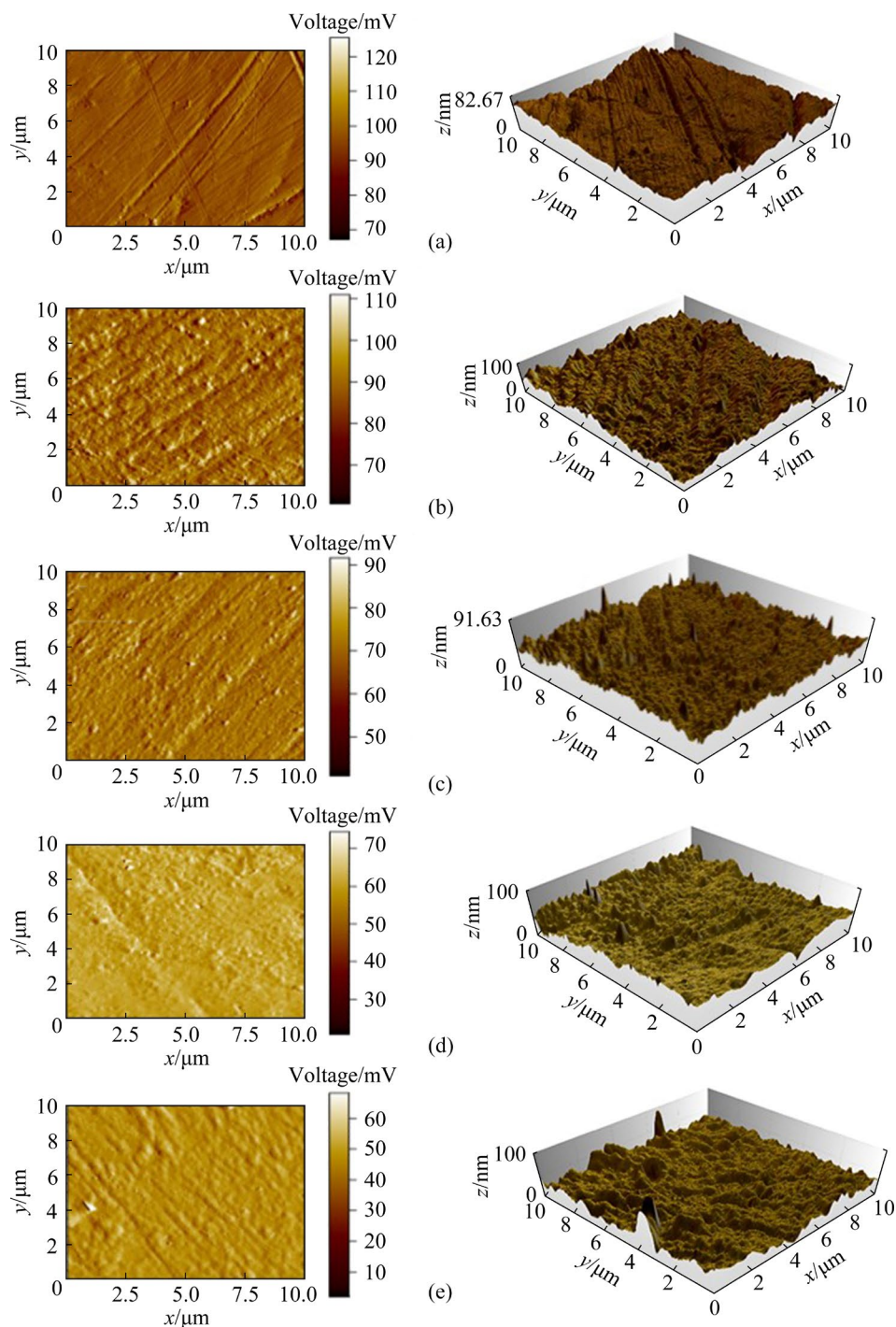


Fig. 2 2D and 3D AFM images of Ti-6Al-4V surfaces after anodization at different DC voltages: (a) Sample 6; (b) Sample 7; (c) Sample 8; (d) Sample 9; (e) Sample 10

the titanium plate to the electrolyte interface at the anode, which thickens the oxide film [48]. The reported surface roughness S_a values in this study were higher than those in some previous works [41,43,45] and somewhat close to others.

BANDEIRA et al [43] concluded that the surface roughness of TiO_2 films deposited on Ti-6Al-4V alloy in oxalic acid slightly increased

with increasing AC voltages, reaching a value of approximately 4.84 nm at 80 V. MALLAIAH and GUPTA [45] observed that the surface of anodized Ti64 alloys was covered with a layer of TiO_2 having sharp peaks and valleys with a roughness value (S_a) of 9 nm, which increased to 33 nm with increasing DC voltages from 10 to 90 V. Other studies [12,13] confirmed the increase of surface roughness and the

Table 4 Surface roughness parameters of anodized two-phase Ti alloys

| Sample No. | S_a/nm | S_q/nm | S_{sk} | S_{ku} |
|------------|-----------------|-----------------|----------|----------|
| 1 | 123.00 | 144.00 | −0.029 | 1.956 |
| 2 | 63.21 | 72.00 | −0.153 | 2.325 |
| 3 | 40.42 | 49.93 | −0.631 | 2.542 |
| 4 | 185.70 | 237.30 | −0.737 | 3.368 |
| 5 | 279.30 | 366.20 | 0.426 | 3.086 |
| 6 | 187.70 | 222.70 | 0.004 | 2.120 |
| 7 | 97.79 | 116.30 | −0.425 | 2.186 |
| 8 | 120.20 | 143.50 | −0.244 | 2.252 |
| 9 | 138.00 | 163.00 | −0.296 | 2.130 |
| 10 | 204.15 | 245.65 | −0.010 | 2.210 |

thickness of TiO_2 coatings with an increase in anodic voltages up to 90 V. However, HOLMBERG et al [41] reported a decrease of R_a (R_a is the average roughness) values of anodized Ti64 alloys with an increase in AC anodization voltages from 1.29 μm at 0 V to around 0.81 μm at 80 V.

It was also noticed from Table 4 that the surface skewness parameter values (S_{sk}) for most of the Ti–6Al–7Nb samples before and after anodization at different voltages were negative values ($S_{sk} < 0$) which revealed that the number of pits or valleys were dominant on the surface as compared to peaks. It was also obvious that the S_{sk} values became more negative with increasing voltages, which implied that the number of valleys increased and became deeper, elevating the surface roughness. However, at an anodization voltage of 80 V, S_{sk} had a positive value ($S_{sk} > 0$), confirming that the surface was dominated with peaks decorated by protrusions rather than valleys. This observation aligns with Fig. 1(e) since the surface was covered with large agglomerated TiO_2 grains.

The surface kurtosis values (S_{ku}) of the first three samples were less than 3, revealing that the surfaces were bumpy. However, at an anodization voltage of 60 V, S_{ku} was higher than 3, which proved that the surface was spiky and dominated by valleys. At 80 V, S_{ku} approached a value of 3 (Gaussian distribution), denoting that elevations and depressions were symmetrical around the mean plane, but the peaks were more prominent due to the positive value of S_{sk} .

Regarding Ti–6Al–4V samples, it was seen from Table 4 that S_{sk} values were negative except

for Sample 6, and S_{ku} values were less than 3 at all anodization voltages, which implied that the surfaces of anodized Ti–6Al–4V alloys were bumpy and dominated with valleys. This was confirmed in Fig. 2 where the cluster of structures or irregularities with increased valleys and peaks were seen on the surfaces.

From the above findings, it is expected that Ti–6Al–7Nb alloy will promote more HA growth on its surface due to its higher roughness parameters compared to its counterpart Ti–6Al–4V alloy.

Typical line profiles from section analysis were generated for anodized Ti–6Al–7Nb and Ti–6Al–4V surfaces and presented in Fig. 3 and Fig. S1 in Supplementary Materials. The profiles were developed by selecting a sectional line from the corresponding 2D AFM image and plotting height data along the surface in the x direction. It was clear from Fig. 3 that the profiles of the lines were somewhat wavy or spiral, the heights of the peaks increased with higher anodization voltages, and the peaks became larger and wider, particularly in Sample 5 (Fig. 3(d)). The observation concerning Sample 5 was in line with the 2D and 3D images of Sample 5 (Fig. 1(e)), where large globular TiO_2 structures were visible on the surface of Ti–6Al–7Nb specimen. The pronounced elevations in the size of the peaks indicated that the thickness and roughness of the TiO_2 films stepped up with the increase in anodization voltages. These results confirmed the higher roughness parameters of the Ti–6Al–7Nb anodized at 60 and 80 V, as shown in Table 4.

On the other hand, Fig. S1 in Supplementary Materials showed that TiO_2 layers deposited on Ti–6Al–4V samples had serrated line profiles across their surfaces. It was seen that the height and width of the peaks of anodized Ti alloys at 60 and 80 V were much smaller than those found on anodized Ti–6Al–7Nb discs at the same voltages (Fig. 3). It was also noticed that the widths of the peaks were narrow, which indicated that the sizes of TiO_2 structures were small, closely packed and nearly uniform. This result implied densification and close packing of relatively small structures formed during nucleation of TiO_2 , making the surface nearly homogenous but with valleys and spikes, and hence serrated texture [28]. These results were compatible with the small-clustered

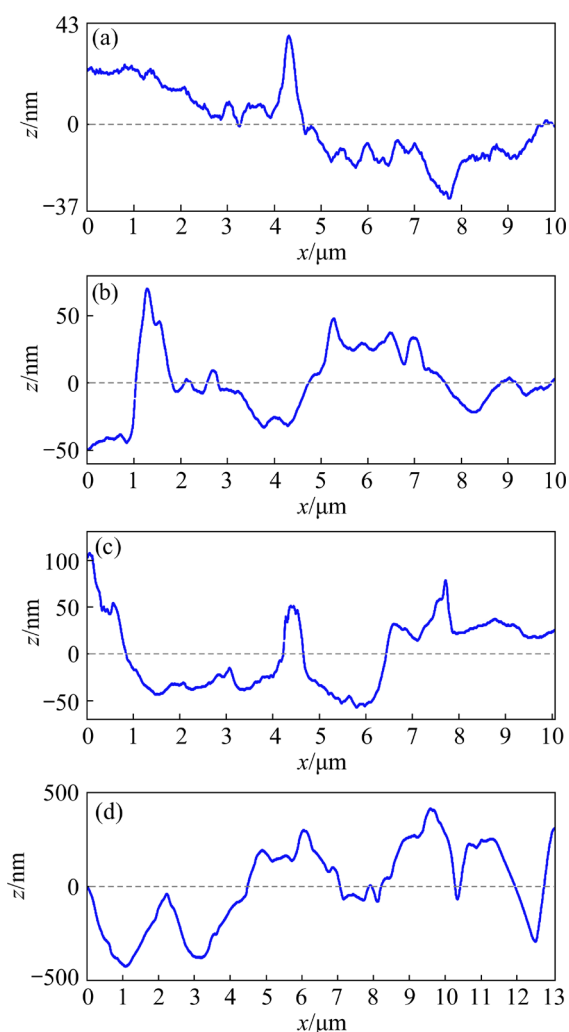


Fig. 3 Line profiles from section analysis for Ti-6Al-7Nb alloys (The heights of the peaks and valleys depend on selected section to be analyzed): (a) Sample 2; (b) Sample 3; (c) Sample 4; (d) Sample 5

structures that were apparent on the surface of anodized Ti-6Al-4V alloys in Fig. 2. Moreover, the line profiles in Fig. S1 in Supplementary Materials confirmed the lower roughness characteristics of anodized Ti-6Al-4V alloys as compared to anodized Ti-6Al-7Nb alloys.

3.3 Surface topography of HA grown on anodized Ti alloys

It was relevant in this work to determine the optimum conditions of anodization which produce TiO_2 coatings with good adhesion and osseointegration properties that further promote the growth of large quantities of HA. 2D and 3D AFM images of deposited HA films on anodized Ti alloys after immersion in SBF for 42 d were shown in Figs. 4 and 5, and their corresponding line profiles

of selected sections were shown in Figs. S2 and S3 in Supplementary Materials. The surface roughness parameters are summarized in Table 5.

It was observed from Fig. 4 that the surface of the Ti-6Al-7Nb sample without anodization was smooth, with a few tiny particles that were seen as very small defined peaks in the 3D image. This means that no HA was precipitated on the surface after immersion in SBF. In Sample 2 (Fig. 4(b)), white HA agglomerated particles, and other scattered small granules were visible on the surface as sharply pointed peaks in the corresponding 3D image. Moreover, Sample 3 was covered with irregular structures that appeared as volcano-shaped distinct peaks in the 3D surface image. A large globular white HA structure and a few other tiny particles were seen on the surface of Sample 4, which appeared as a large bump in the 3D image. On the other hand, Sample 5 showed increased growth of white HA dense globular structures, almost covering the whole surface, and housing the large TiO_2 hemispherical grains. It can be suggested from the observed results that the quantity of deposited HA increased with the increase in the anodization voltage of the modified Ti alloys and that the Ti-6Al-7Nb alloy anodized at 80 V had the greatest susceptibility to the formation of large quantities of HA on its surface, which makes it the most appropriate alloy with better osseointegration properties as compared to the other anodized Ti-6Al-7Nb alloys.

Figure 5 showed the HA deposited on the surface of anodized Ti-6Al-4V alloys. It was clear that a couple of small white HA aggregated particles appeared on the surface of Sample 6 (Ti-6Al-4V alloy without anodization). Different sizes of assembled white HA masses were scattered all over the surfaces of Samples 8 and 9, which increased with an increase in the anodization voltages. However, Sample 10 (Ti-6Al-4V alloy anodized at 80 V) showed a homogeneous surface with inclined projections and large aggregated masses of HA appearing at some parts of the surface.

It was noticed from Table 5 that S_a roughness values for all anodized Ti samples decreased when HA was deposited on their surfaces after immersion in SBF. This could be ascribed to the incorporation of HA into oxide films, which led to the stabilization of the TiO_2 coatings. Moreover, the diffusion of HA into the valleys that were present on the surface of

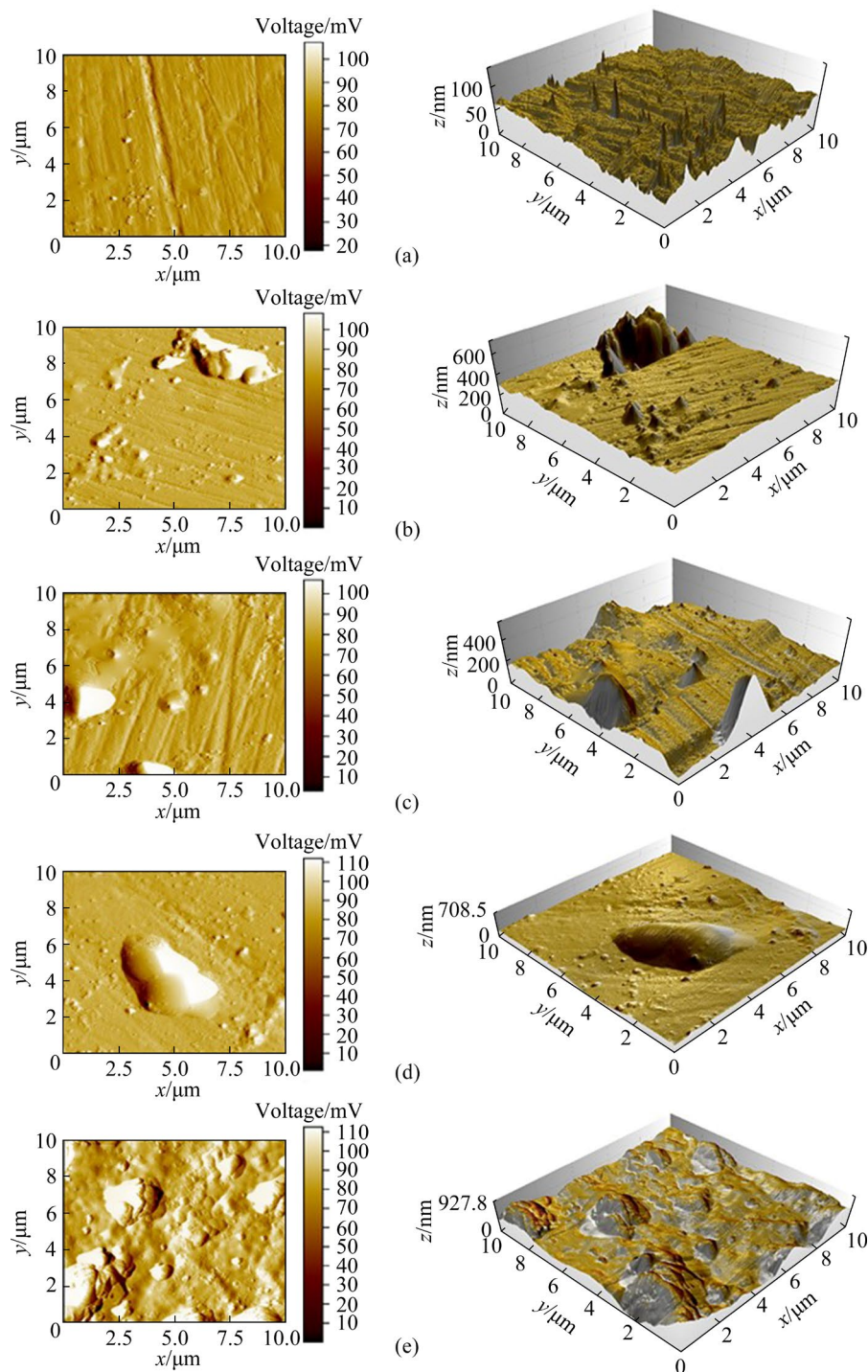


Fig. 4 2D and 3D AFM images of HA particles deposited on anodized Ti-6Al-7Nb surfaces: (a) Sample 1; (b) Sample 2; (c) Sample 3; (d) Sample 4; (e) Sample 5

anodized Ti alloys decreased the structural defects of the TiO_2 films and broadened the peaks, which led to smoother surfaces. It was clear that the surface properties of the HA layer were highly dependent on the surface morphology and roughness properties of the Ti oxide layers.

Table 5 showed that S_a values for Samples 1–3

of Ti-6Al-7Nb alloy initially decreased from 59.42 to 46.85 nm and then increased again for Samples 4 (anodized at 60 V) and 5 (anodized at 80 V) until it reached 246.80 nm. This behavior was in accordance with the behavior of roughness properties of the TiO_2 films deposited on Ti-6Al-7Nb discs with increasing anodization voltages.

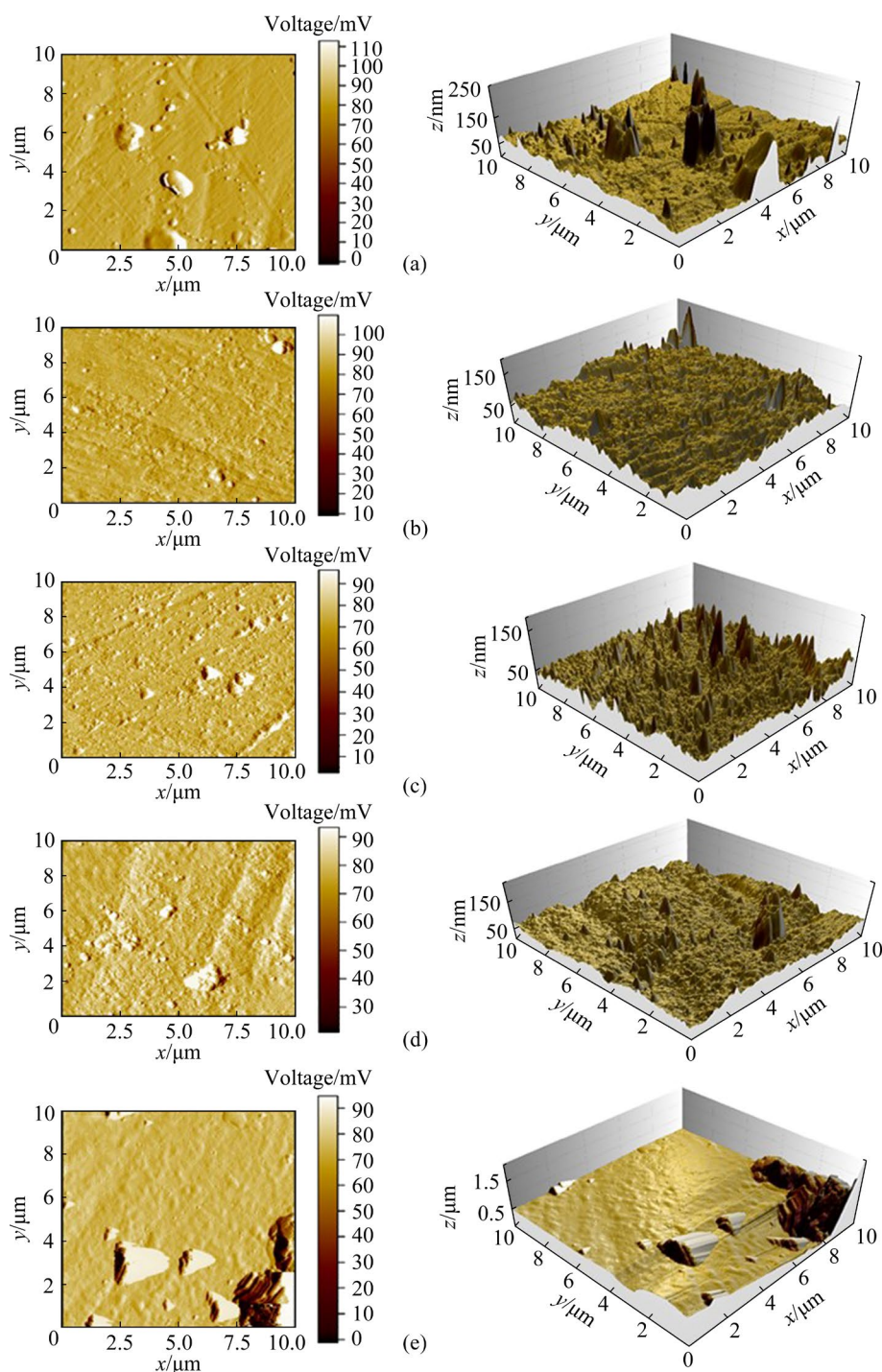


Fig. 5 2D and 3D AFM images of HA particles deposited on anodized Ti-6Al-4V surfaces: (a) Sample 6; (b) Sample 7; (c) Sample 8; (d) Sample 9; (e) Sample 10

The high S_a for HA deposited on Sample 5 was attributed to the high surface roughness and presence of hills and valleys on the surface of the oxide coating which provided good adhesion properties and enhanced the development of HA. Hence, the roughness features and morphologies of the TiO_2 layers for all Ti-6Al-7Nb samples were

reflected on the nature and the amount of deposited HA.

However, Ti-6Al-4V alloys showed different behaviors where S_a values initially decreased from 93.72 nm for Sample 6 (without anodization) to 60.64 nm for Sample 7 (anodized at 20 V). An increase in roughness parameter was observed for

Table 5 Surface roughness parameters of HA layers deposited on anodized Ti alloy samples

| Sample No. | S_a /nm | S_q /nm | S_{sk} | S_{ku} |
|------------|-----------|-----------|----------|----------|
| 1 | 59.42 | 68.79 | −0.032 | 1.936 |
| 2 | 57.62 | 85.68 | 2.048 | 10.920 |
| 3 | 46.85 | 55.65 | 0.236 | 3.039 |
| 4 | 155.50 | 194.30 | 0.367 | 2.479 |
| 5 | 246.80 | 296.40 | 0.263 | 2.712 |
| 6 | 93.72 | 111.10 | 0.075 | 2.107 |
| 7 | 60.64 | 74.56 | −0.480 | 2.847 |
| 8 | 121.22 | 142.90 | −0.138 | 2.219 |
| 9 | 80.55 | 99.93 | −0.362 | 2.895 |
| 10 | 181.80 | 234.90 | 0.966 | 4.988 |

Sample 8, where S_a was 121.22 nm, then it decreased for Sample 9 to 80.55 nm, and finally, the highest S_a value was 181.80 nm for Sample 10 (anodized at 80 V). Despite the high surface roughness of Sample 10 as opposed to the other Ti–6Al–4V anodized alloys, however, the surface was partially covered with HA agglomerations, which grew only on one part of the surface and were not distributed on the rest of the surface. This implied that this anodization voltage was not favorable for HA precipitation.

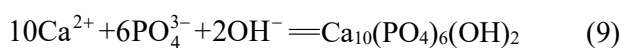
Furthermore, the surface skewness parameters (S_{sk}) for all HA layers deposited on the anodized Ti–6Al–7Nb samples after immersion in SBF had positive values which were in contrast with their negative values before immersion, which suggested that the valleys on the surface of the anodized Ti alloys were filled with HA layers or agglomerations along with flattening of some peaks due to coverage of HA which accordingly caused the surface to be smoother than before. This led to the domination of peaks over valleys, and the positive values of S_{sk} . The surface kurtosis values (S_{ku}), which measure the spikiness of height distribution of the surface, differed from one sample to another. Samples 1, 4, and 5 showed S_{ku} values below 3, which implied that the surfaces were bumpy, as was obvious in the 3D images in Fig. 5. However, the S_{ku} values for Sample 2 were much higher than 3 and it approached a value of 3 for Sample 3 (Gaussian distribution). The high S_{ku} value for Sample 2 was probably due to the presence of sharp pointed peaks that appeared on the surface which made the surface spiky.

On the other hand, the S_{sk} values for the HA layers deposited on Ti–6Al–4V alloys revealed that the surfaces were all prominent with valleys for Samples 7–9 and with peaks for Samples 6 and 10. The S_{ku} values suggested that the surfaces were bumpy for all Ti samples except Sample 10 where S_{ku} was higher than 3, denoting that the surface was spiky due to the sharp inclined projections that was seen on the surface.

Sectional line profiles were also performed for HA formed on the anodized Ti–6Al–7Nb and Ti–6Al–4V surfaces and presented in Figs. S2 and S3 in Supplementary Materials. It was obvious that the peaks of HA structures developed on the surface of Ti–6Al–7Nb alloys (Fig. S2) were broader than those formed on Ti–6Al–4V alloys (Fig. S3) both in height and diameter, which indicated the increase in the size of surface grains or aggregations formed on the former alloy and hence rise in its surface roughness which agreed with the results in Table 5. This also indicated that there was growth of HA nuclei resulting in densification of large HA particles on the surfaces of these alloys. Moreover, Fig. S2 showed that the surfaces of the Ti–6Al–7Nb specimens were dominated by large-sized peaks, which were compatible with the skewness values in Table 5. On the other hand, Fig. S3 showed that the peaks were small in size and close to each other, revealing that the small-sized HA structures were formed on the surfaces of Ti–6Al–4V alloys. The morphologies of the surfaces were dominated by valleys with few pronounced peaks, particularly in (Fig. S3(d)). These observations also complied with the skewness values in Table 5.

It can be concluded from the above results that Sample 5 was the most suitable sample for HA development on its surface. This suggested that an anodization voltage of 80 V was favorable for the increased formation of HA on the Ti–6Al–7Nb alloy, and it enhanced the spreading of HA on the entire surface. The increase in HA growth on the Ti alloy's surface is considered one-factor promoting osseointegration since it increases strength between the alloy and the surrounding bones and improves implant fixation, leading to long-term stability inside the body. However, for the Ti–6Al–4V alloy, it was seen that an anodization voltage of 40 V (Sample 8) was favorable for promoting HA growth distributed on its surface, although the quantities are less than those of its counterpart alloy.

The increased HA formation capability of anodized Ti–6Al–7Nb alloys can be due to the existence of Nb in the structure of the alloy. It was previously reported that the presence of Nb as β stabilizing element instead of vanadium improved the alloy's ability to form HA on its surface [31,32]. The formation of HA on the surface of the anodized Ti alloys in SBF can be explained as follows: Ca^{2+} ions present in the body fluid penetrated into the TiO_2 oxide layers, which was derived by the concentration difference and, therefore, developed a positive charge on its surface [49]. This helps the titanium surface to absorb PO_4^{3-} ions and initiate HA nucleation according to Reaction (9). The homogeneous nucleation of calcium phosphate triggers the deposition of HA crystals. The growth of HA crystals further promotes the formation of agglomerated HA particles.



Furthermore, MASAHASHI et al [50] mentioned that the establishment of HA on the surface of anodized Ti–Nb–Sn alloy was due to the penetration of Ca and P, which are the main constituents of HA present in the body fluid, into the pores of the TiO_2 oxide layers as Ca^{2+} and P^{5+} (as H_2PO_4^-) and the consecutive formation of HA.

Concerning the pH, a slight increase in pH was recorded from 7.4 to 7.5–7.7 for all investigated samples after immersion for 42 d, which showed that it was not a prominent factor in this study. However, it is worth noting that in-vivo conditions constantly change regarding temperature and pH that could affect HA formation and osseo-integration.

Anodized Ti alloys (Samples 5 and 8) were selected for further SEM and EDS analysis to determine more information on the morphology and

elemental analysis of the precipitated HA phases on the surface of anodized Ti alloys after submersion in SBF. Sample 5 (Ti–6Al–7Nb alloy anodized at 80 V) was chosen because it produced the highest yields of HA structures with excellent surface coverage. On the other hand, Sample 8 (Ti–6Al–4V alloy anodized at 40 V) was selected since it provided HA coverage in many parts of the surface but with lower HA quantities than Sample 5.

3.4 SEM images

3.4.1 SEM images of forged samples before anodization

The microstructures of the as-forged Ti–6Al–7Nb and Ti–6Al–4V specimens before anodization are shown in Fig. 6. As visualized, the microstructure of the forged samples consisted of fine equiaxed grains of α and some β phases.

3.4.2 SEM images of HA deposited on anodized Ti alloys

Figure 7 shows SEM images of HA deposited on the surfaces of the selected anodized Ti alloy samples after immersion in SBF for 42 d. It was clear from Figs. 7(a, b) that the surface of the anodized Ti–6Al–7Nb alloy (Sample 5) was almost fully covered with dense agglomerated white HA masses or deposits, while Figs. 7(c, d) implied that the surface of the anodized Ti–6Al–4V alloy (Sample 8) was partially covered with ring-like white HA structures. This observation implied that a large amount of HA nucleation was developed on the surface of the Ti–6Al–7Nb alloy, which further demonstrated its excellent osseointegration properties and increased susceptibility to promoting HA formation. These conclusions were compatible with the AFM results in Figs. 4(e) and 5(c) where the surface of Sample 5 was seen to be almost fully covered with large HA agglomerations (Fig. 4(e)),

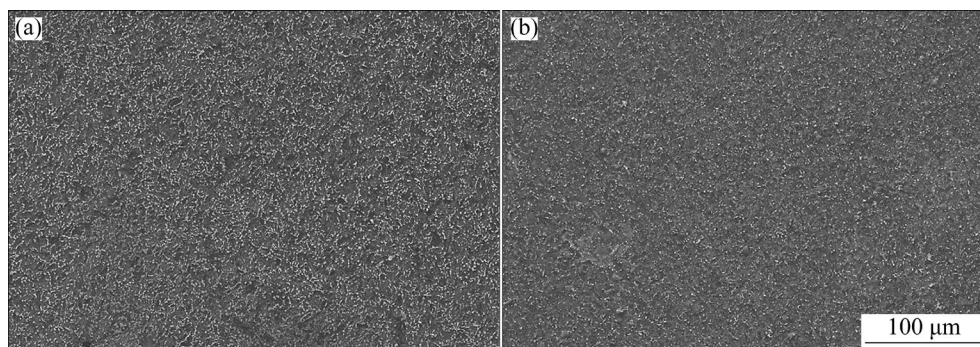


Fig. 6 SEM images of forged Ti–6Al–7Nb (a) and Ti–6Al–4V (b) specimens before anodization

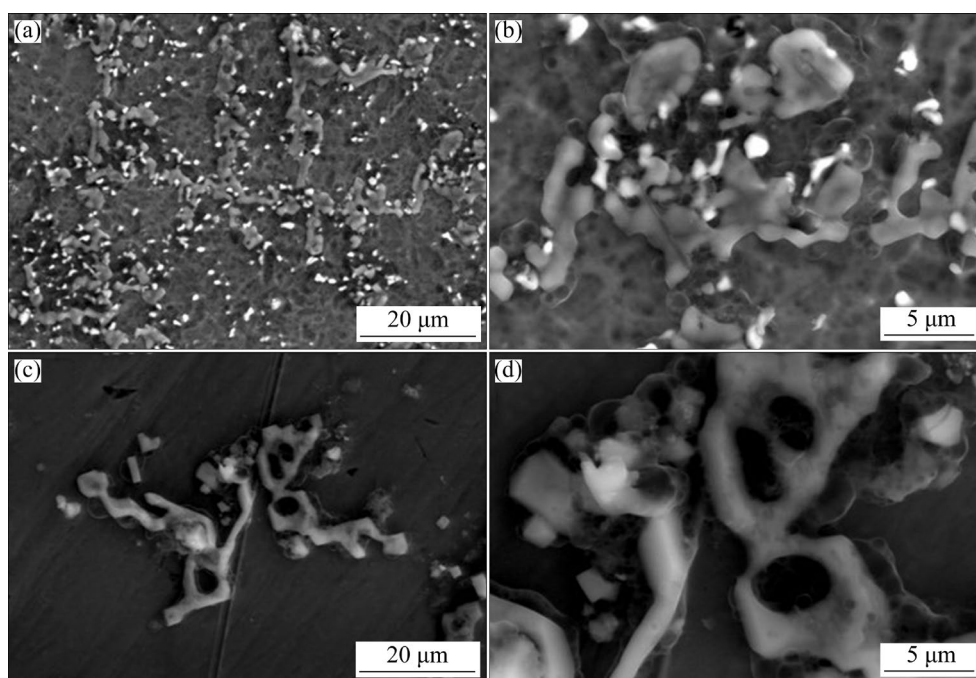


Fig. 7 SEM images of HA formed on surface of Ti alloys: (a, b) Sample 5; (c, d) Sample 8

while HA small, aggregated particles were dispersed on the surface of Sample 8 (Fig. 5(c)). It can also be visible from Fig. 7 that the surface morphology of the uncovered TiO_2 layer on Sample 5 was somewhat porous due to the anodization process that created micro and nano porous structures [51], which helped the adhesion and growth of HA into its pores and on the surface. However, the texture of the oxide layer on Sample 8 was nearly homogeneous, reducing its liability to grow HA. It is clear from the above outcomes that the surface topography of anodized Ti alloys greatly influenced HA structure growth. KRČIL et al [52,53] investigated the effect of TiO_2 layers developed on the surfaces of CP titanium (Grade 2), Ti–6Al–4V, and Ti–39Nb alloys by anodization at higher voltages (100 V) in H_2SO_4 electrolyte solution. They found that the morphologies of the oxide layers affected the biocompatibility and the growth rates of HA.

To determine the elemental composition and to verify the existence of Ca and P on the surface of the two types of alloys, EDS measurements were further performed and displayed in Fig. 8. Figure 8(a) clarified the presence of the basic components of the alloy (Ti, Nb, and Al) while Fig. 8(b) showed the presence of Ti, V, and Al. Moreover, EDS analysis revealed the existence of

Ca and P on the surface of both anodized alloys; other peaks of O, Na, Mg, Cl, C, K, and N were also present. The detection of Ti and O elements proved the existence of TiO_2 films on the surface of the specimens. Moreover, Ca/P molar ratios calculated from EDS measurements were 1.44 for Sample 5 and 0.94 for Sample 8. Although the optimal Ca/P molar ratio for stoichiometric HA is 1.67, stable HA phases have been found to persist in a Ca/P molar range of 1.3 to 1.8 [54,55]. It was previously reported that HA was found to be calcium deficient with Ca/P molar ratios lower than 1.67 and greater than 1.33 [56,57]. It was also mentioned that HA in bone is usually calcium deficient, with a Ca/P molar ratio lower than 1.67 and close to 1.5 [58], and it is usually substituted with ions like Mg^{2+} , Na^+ , K^+ or groups such as carbonates (CO_3^{2-}) [46]. This decreases the value of the Ca/P molar ratio of the stoichiometric HA [59]. The Ca/P molar ratio of 1.44 in this work (which is higher than 1.3 and close to 1.5) verifies the existence of calcium deficient HA on the surface of Sample 5, which complies with a study presented by RADTKE et al [46], who produced titanium dioxide nanotubes/hydroxyapatite nanocomposites on titanium alloys. The authors confirmed the existence of HA films with Ca/P molar ratios in the range of (1.45–1.62).

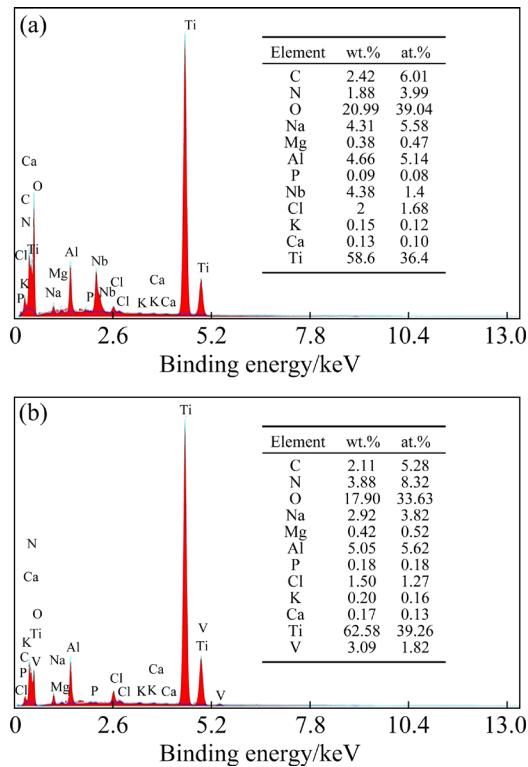


Fig. 8 EDS analysis results of HA formed on anodized Ti alloys: (a) Sample 5; (b) Sample 8

However, the low Ca/P molar ratio of 0.94 of Sample 8 could be correlated to the formation of HA having very low Ca concentrations with respect to P and hence lowering its Ca/P molar ratios or the development of dicalcium phosphate compounds on

the surface of Sample 8. PAVLOVIĆ et al [55] studied the synthesis of HA/TiO₂ coatings on titanium alloys by means of anaphoretic deposition of HA and proved the coexistence of HA in the coatings having a Ca/P molar ratio range of 1.19–1.75. They related the low Ca/P molar ratios to the abrupt crystalline lattice of HA. In addition, it was proved that calcium phosphates or mixtures of apatites having Ca/P molar ratios not equal to 1.67 also promote the formation of new bone tissues [60].

Figures 9 and 10 represent the EDS mappings of HA developed on the surfaces of the alloys. It was evident that calcium and phosphorus which are the main constituents of HA were apparent on both samples and they were distributed on the entire surfaces of the alloys. It was also obvious that Na and Cl elements appeared on certain parts of the surfaces which revealed the formation of some salts in certain regions.

3.4.3 Thickness of HA layers formed on surfaces of anodized Ti alloys

The thickness of the HA layers developed on the surfaces of selected modified Ti–6Al–7Nb (Samples 3 and 5) was analyzed using SEM, and images of the cross sections are presented in Fig. 11. It was apparent that there was a significant difference between the thicknesses of HA layers deposited on both samples and that anodization of this type of alloy originated an increase in the

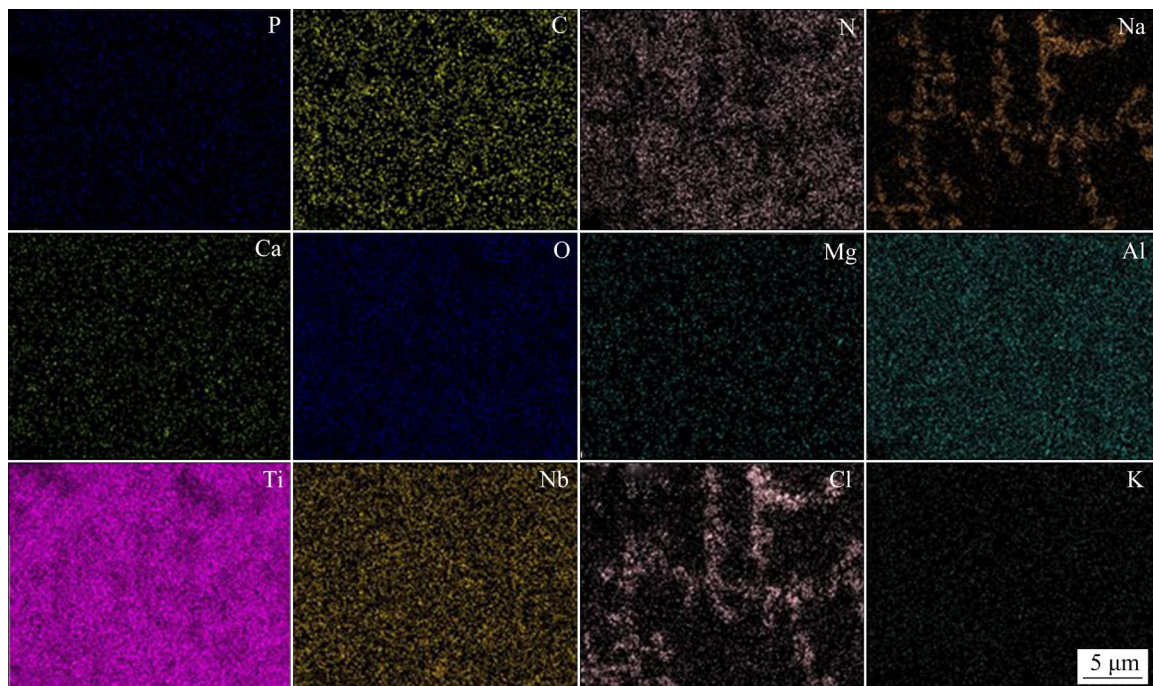


Fig. 9 Surface elemental mappings for HA formed on surface of Sample 5

thickness of HA and a potential of 80 V greatly enhanced the formation of HA. Figure 11(a) revealed that the HA layer precipitated on Sample 3 had a mean thickness of $(10.65 \pm 0.87) \mu\text{m}$ and that the uncovered oxide layer was highly porous which proved the existence of porous TiO_2 films on the surface of the anodized Ti alloys. However, the thicknesses of the TiO_2 anodic films were not

apparent in the SEM image due to the development of very thin oxide layers. Due to the differences in the thickness of HA layers developed on Sample 5, it was relevant to take different SEM images in different regions of the surface with different magnifications to have an overview of the HA layers on the entire surface. Figure 11(b) showed a general outlook of the precipitated HA layer on

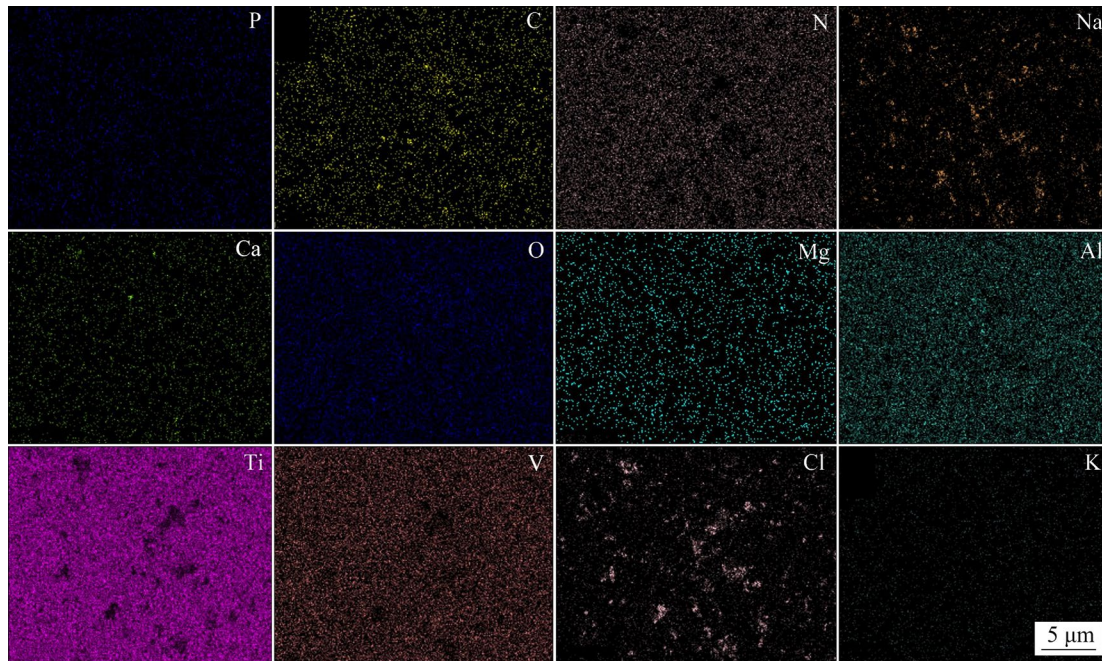


Fig. 10 Surface elemental mappings for HA formed on surface of Sample 8

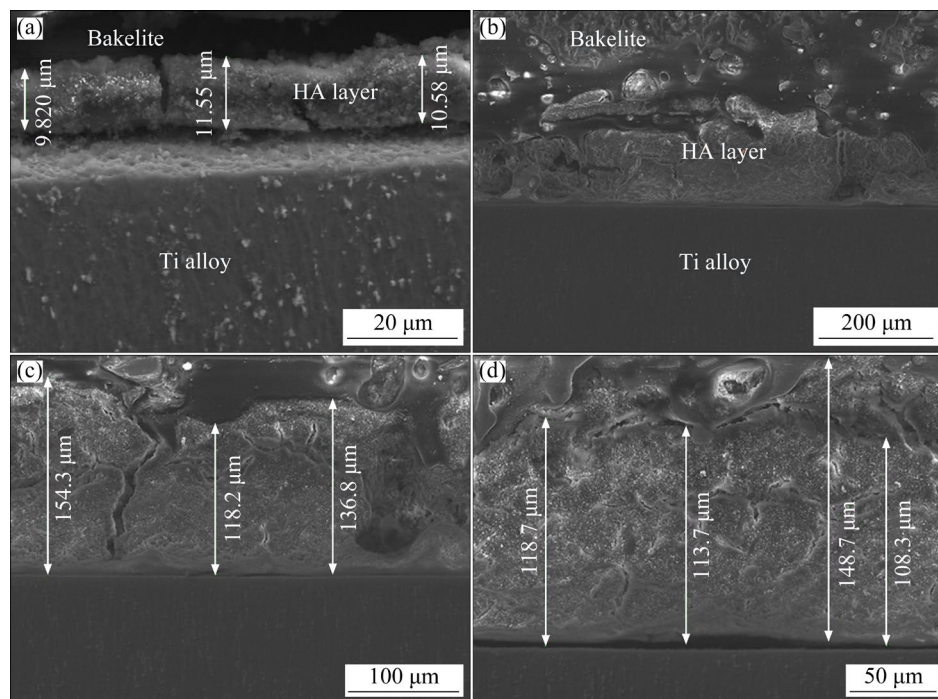


Fig. 11 SEM images of cross-sections of HA layers on surface of Ti-6Al-7Nd alloys: (a) HA deposited on Sample 3; (b–d) Three magnifications of HA deposited on Sample 5

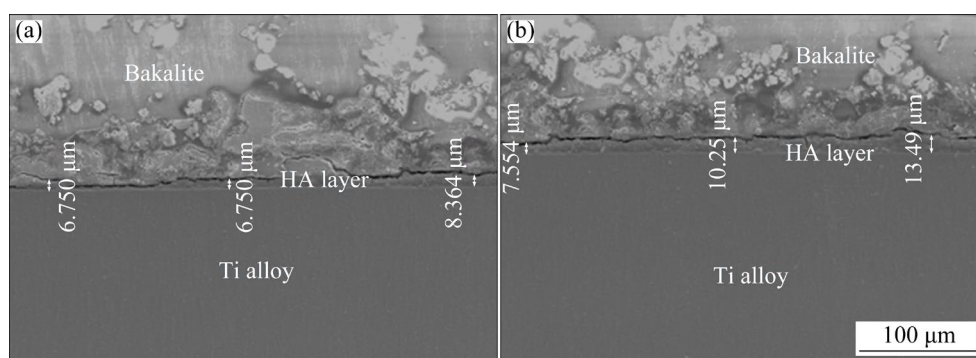


Fig. 12 SEM images of cross-sections of HA layers on surface of Ti-6Al-4V alloys: (a) HA deposited on Sample 7; (b) HA deposited on Sample 8

Sample 5, the mean thickness of HA layer was $(128.38 \pm 18.13) \mu\text{m}$, as seen from Figs. 11(b) and (c) which signified the excellent bone formation abilities of Ti-6Al-7Nb alloy anodized at 80 V.

Figure 12 showed the SEM images of cross-sections of HA layers deposited on Ti-6Al-4V alloys (Samples 7 and 8). It was obvious that there was not much difference between the thicknesses of HA developed on both alloys anodized at different voltages, which revealed that anodization had no obvious effect on the deposition of HA. The mean thickness of HA developed on Sample 7 was $(7.28 \pm 0.93) \mu\text{m}$ and that formed on sample 8 was found to be $(10.43 \pm 2.97) \mu\text{m}$. These observations confirmed that the Ti-6Al-7Nb anodized at 80 V was the most adequate alloy for HA growth on its surface since it induced the formation of HA layer with a higher thickness than that formed on the other explored alloys. This outstanding capacity for HA formation demonstrates that this alloy is very suitable for bone implants and can highly facilitate binding to the surrounding bone tissues in in-vivo conditions.

To confirm the existence of calcium and phosphorus in the HA layer on Sample 5, EDS analysis was performed for the HA layer shown in Fig. 11(b) and presented in Fig. S4 in Supplementary Materials. It was clear that the calcium and phosphorus ions were present along with the basic elements of the alloy.

Future comparative studies could be conducted on alternative methods to produce HA films on the Ti-6Al-7Nb alloy presented in this work including RF magnetron sputtering, plasma spraying, and sol-gel to evaluate the bone bonding capabilities of these excellent groups of alloys. Also, forthcoming

investigations regarding energy, wettability analysis and adhesion of titanium dioxide layer are planned, since it might be crucial for any practical use.

4 Conclusions

(1) This work aimed to investigate the influence of anodization voltages on the surface topography of Ti-6Al-7Nb and Ti-6Al-4V alloys and to explore the optimum conditions that produce TiO_2 films with increased surface roughness and thus bone forming ability.

(2) The S_a values of surface roughness of TiO_2 films deposited on Ti-6Al-7Nb alloys were superior to those of Ti-6Al-4V alloys, which makes them more suitable for bone applications since rougher surfaces enable bone ingrowth for orthopedic implants.

(3) Ti-6Al-7Nb specimens showed increased potential for HA growth after being immersed in SBF for 42 d compared to Ti-6Al-4V specimens, which suggests its promising performance as orthopedic implants.

(4) The surface of Ti-6Al-7Nb alloy anodized at 80 V produced the highest yields of HA aggregations with outstanding surface coverage and a mean thickness of $(128.38 \pm 18.13) \mu\text{m}$, making it the most convenient alloy having the highest susceptibility to the growth of HA on its surface. This implies enhanced bone integration and long service life inside the living body.

(5) Amongst the anodized Ti-6Al-4V alloys, it was seen that a voltage of 40 V provided the most suitable HA surface coverage.

(6) Despite the high roughness of Ti-6Al-4V specimens anodized at 80 V, the surface was not

fully covered by HA agglomerates, which is not favorable for bone osseointegration.

(7) Future work may include research on alternative techniques for developing HA coatings on the suggested Ti–6Al–7Nb alloy, such as RF magnetron sputtering, plasma spraying, and sol–gel. Other factors such as energy, wettability studies, and the adherence of the titanium dioxide layer are also planned since it may be relevant for any practical use.

CRedit authorship contribution statement

Rania E. HAMMAM: Contribute to the electrochemical anodization, optical, SEM and AFM characterization and take the lead in writing the manuscript; **Engie M. SAFWAT:** Contribute to the immersion experimentation, AFM inspection and characterization; **Soha A. ABDEL-GAWAD:** Contribute to electrochemical anodization, optical characterization and supervision of the manuscript; **Madiha SHOEIB:** Conceive and plan the electrochemical anodization, contribute to SEM, AFM characterization and supervision of the manuscript; **Shimaa EL-HADAD:** Devise the conceptual design, microstructure characterization and supervision of the manuscript. All authors contributed to critical analysis, writing and revising the manuscript.

Declaration of competing interest

The authors declare that they have no known competing financial interests or personal relationships that could have appeared to influence the work reported in this paper.

Acknowledgments

The authors would like to acknowledge the financial support from the Science and Technology Development Fund of Egypt (No. 5540).

Supplementary Materials

Supplementary Materials in this paper can be found at: http://tnmsc.csu.edu.cn/download/13-p3629-2023-0647-Supplementary_Materials.pdf.

References

- [1] ÖZCAN M, HÄMMERLE C. Titanium as a reconstruction and implant material in dentistry: Advantages and pitfalls [J]. *Materials*, 2012, 5: 1528–1545.
- [2] BÜTEV E, ESEN Z, BOR Ş. Characterization of Ti₆Al₇Nb alloy foams surface treated in aqueous NaOH and CaCl₂ solutions [J]. *Journal of the Mechanical Behavior of Biomedical Materials*, 2016, 60: 127–138.
- [3] STEINEMANN S G. Corrosion of surgical implants—In vivo and in vitro tests, evaluation of biomaterials [J]. New York: Wiley, 1980: 1–34.
- [4] LIU X Y, CHU P K, DING C X. Surface modification of titanium, titanium alloys, and related materials for biomedical applications [J]. *Materials Science and Engineering R*, 2004, 47: 49–121.
- [5] OKAZAKI Y. *Metals for biomedical devices* [M]. Amsterdam: Elsevier, 2019: 31–94.
- [6] EL-HADAD S, SAFWAT E M, SHARAF N F. In-vitro and in-vivo, cytotoxicity evaluation of cast functionally graded biomaterials for dental implantology [J]. *Materials Science and Engineering C*, 2018, 93: 987–995.
- [7] KONATU R T, DOMINGUES D D, ESCADA A L A, CHAVES J A M, NETIPANYJ M F D, NAKAZATO R Z, POPAT K C, GRANDINI C R, ALVES CLARO A P R. Synthesis and characterization of self-organized TiO₂ nanotubes grown on Ti–15Zr alloy surface to enhance cell response [J]. *Surfaces and Interfaces*, 2021, 26: 101439.
- [8] CHERNOZEM R V, SURMENEVA M A, IGNATOV V P, PELTEK O O, GONCHARENKO A A, MUSLIMOV A R, TIMIN A S, TYURIN A I, IVANOV Y F, GRANDINI C R, SURMENEV R A. Comprehensive characterization of titania nanotubes fabricated on Ti–Nb alloys: Surface topography, structure, physicochemical behavior, and a cell culture assay [J]. *ACS Biomaterials Science and Engineering*, 2020, 6: 1487–1499.
- [9] ZIELIŃSKI A, ANTONIUK P, KRZYSZTOFOWICZ K. Nanotubular oxide layers and hydroxyapatite coatings on Ti–13Zr–13Nb alloy [J]. *Surface Engineering*, 2014, 30: 643–649.
- [10] STRNAD G, JAKAB-FARKAS L, GOBBER F S, PETER I. Synthesis and characterization of nanostructured oxide layers on Ti–Nb–Zr–Ta and Ti–Nb–Zr–Fe biomedical alloys [J]. *Journal of Functional Biomaterials*, 2023, 14: 180.
- [11] STOILOV M, STOILOV L, ENKLING N, STARK H, WINTER J, MARDER M, DOMINIK K. Effects of different titanium surface treatments on adhesion, proliferation and differentiation of bone cells: An in vitro study [J]. *Journal of Functional Biomaterials*, 2022, 13: 143.
- [12] ZHANG W X, GU J P, ZHANG C, XIE Y T, ZHENG X B. Preparation of titania coating by induction suspension plasma spraying for biomedical application [J]. *Surface and Coatings Technology*, 2019, 358: 511–520.
- [13] DOMÍNGUEZ-TRUJILLO C, PEÓN E, CHICARDI E, PÉREZ H, RODRÍGUEZ-ORTIZ J A, PAVÓN J J, GARCÍA- COUCE J, GALVAN J C, GARCÍA-MORENO F, TORRES Y. Sol–gel deposition of hydroxyapatite coatings on porous titanium for biomedical applications [J]. *Surface and Coatings Technology*, 2018, 333: 158–162.
- [14] AYDIN I, BAHÇEPINAR A I, KIRMAN M, ÇİPİLOĞLU M A. HA coating on Ti₆Al₇Nb alloy using an electrophoretic deposition method and surface properties examination of the resulting coatings [J]. *Coatings*, 2019, 9: 402.
- [15] CHO Y S, LIAO L K, HSU C H, HSU Y H, WU W Y, LIAO S C, CHEN K H, LUI P W, ZHANG S, LIEN S Y. Effect of substrate bias on biocompatibility of amorphous carbon coatings deposited on Ti₆Al₄V by PECVD [J]. *Surface and Coatings Technology*, 2019, 357: 212–217.
- [16] KUMAR A, KUSHWAHA M K. Surface modification of titanium alloy by anodic oxidation method to improve its biocompatibility [J]. *Current Science*, 2021, 120: 907–914.

- [17] MANJIAH M, LAUBSCHER R F. Effect of anodizing on surface integrity of Grade 4 titanium for biomedical applications [J]. *Surface and Coatings Technology*, 2017, 310: 263–272.
- [18] KHAW J S, CURIONI M, SKELDON P, BOWEN C R, CARTMELL S H. A novel methodology for economical scale-up of TiO₂ nanotubes fabricated on Ti and Ti alloys [J]. *Journal of Nanotechnology*, 2019, 2019: 38–40.
- [19] AHMADI S, RIAHI Z, ESLAMI A, SADRNEZHAAD S K. Fabrication mechanism of nanostructured HA/TNTs biomedical coatings: An improvement in nanomechanical and in vitro biological responses [J]. *Journal of Materials Science: Materials in Medicine*, 2016, 27: 150.
- [20] GUO T Q, IVANOVSKI S, GULATI K. Fresh or aged: Short time anodization of titanium to understand the influence of electrolyte aging on titania nanopores [J]. *Journal of Materials Science & Technology*, 2022, 119: 245–256.
- [21] SWAMI N, CUI Z W, NAIR L S. Titania nanotubes: Novel nanostructures for improved osseointegration [J]. *Journal of Heat Transfer*, 2011, 133: 034002.
- [22] KOKUBO T, TAKADAMA H. How useful is SBF in predicting in vivo bone bioactivity? [J]. *Biomaterials*, 2006, 27: 2907–2915.
- [23] CIOBANU M G, POP G, CIOBANU O. Hydroxyapatite coatings on titanium implants [J]. *Revista de Chimie*, 2007, 58: 1313–1315.
- [24] DOMÍNGUEZ-TRUJILLO C, TERNERO F, RODRÍGUEZ-ORTIZ J A, HEISE S, BOCCACCINI A R, LEBRATO J, TORRES Y. Bioactive coatings on porous titanium for biomedical applications [J]. *Surface and Coatings Technology*, 2018, 349: 584–592.
- [25] HE D H, WANG P, LIU P, LIU X K, MA F C, ZHAO J. HA coating fabricated by electrochemical deposition on modified Ti₆Al₄V alloy [J]. *Surface and Coatings Technology*, 2016, 301: 6–12.
- [26] STĘPIEŃ M, HANDZLIK P, FITZNER K. Electrochemical synthesis of oxide nanotubes on Ti₆Al₇Nb alloy and their interaction with the simulated body fluid [J]. *Journal of Solid State Electrochemistry*, 2016, 20: 2651–2661.
- [27] CHERNOZEM R V, SURMENEVA M A, KRAUSE B, BAUMBACH T, IGNATOV V P, TYURIN A I, LOZA K, EPPEL M, SURMENEV R A. Hybrid biocomposites based on titania nanotubes and a hydroxyapatite coating deposited by RF-magnetron sputtering: Surface topography, structure, and mechanical properties [J]. *Applied Surface Science*, 2017, 426: 229–237.
- [28] MWEMA F M, OLADIJO O P, SATHIARAJ T S, AKINLABI E T. Atomic force microscopy analysis of surface topography of pure thin aluminum films [J]. *Materials Research Express*, 2018, 5: 046416.
- [29] ERINOSH M F, AKINLABI E T. Estimation of surface topography and wear loss of laser metal-deposited Ti₆Al₄V and Cu [J]. *Advanced Engineering Materials*, 2016, 18: 1396–1405.
- [30] KWOKA M, OTTAVIANO L, SZUBER J. AFM study of the surface morphology of L-CVD SnO₂ thin films [J]. *Thin Solid Films*, 2007, 515: 8328–8331.
- [31] ZAKI A, EL-HADAD S, KHALIFA W. Surface modification effects on microstructure and mechanical properties of bio-titanium alloys [M]. *Materials Science Forum*, 2017, 909: 199–204.
- [32] ABDEL-SALAM M, EL-HADAD S, KHALIFA W. Effects of microstructure and alloy composition on hydroxyapatite precipitation on alkaline treated α/β titanium alloys [J]. *Materials Science and Engineering C*, 2019, 104: 109974.
- [33] MARTINEZ A L, FLAMINI D O, SAIDMAN S B. Corrosion resistance improvement of Ti–6Al–4V alloy by anodization in the presence of inhibitor ions [J]. *Transactions of Nonferrous Metals Society of China*, 2022, 32: 1896–1909.
- [34] SUL Y T, JOHANSSON C B, JEONG Y, ALBREKTSSON T. The electrochemical oxide growth behaviour on titanium in acid and alkaline electrolytes [J]. *Medical Engineering & Physics*, 2001, 23: 329–346.
- [35] AL-RADHA D A S D. Anodization and Titanium Surface Topography [J]. *International Journal of Science and Research*, 2017, 6: 2000–2004.
- [36] ALIPAL J, LEE T C, KOSHY P, ABDULLAH H Z, IDRIS M I. Evolution of anodised titanium for implant applications [J]. *Heliyon*, 2021, 7: e07408.
- [37] İZMİR M, ERCAN B. Anodization of titanium alloys for orthopedic applications [J]. *Frontiers of Chemical Science and Engineering*, 2019, 13: 28–45.
- [38] PILIPENKO A, MAIZELIS A, PANCHEVA H, ZHELAVSKA Y. Electrochemical oxidation of VT6 titanium alloy in oxalic acid solutions [J]. *Chemistry and Chemical Technology*, 2020, 14: 221–226.
- [39] BAINO F, YAMAGUCHI S. The use of simulated body fluid (SBF) for assessing materials bioactivity in the context of tissue engineering: Review and challenges [J]. *Biomimetics*, 2020, 5: 57.
- [40] YONG Q, CHANG J, LIU Q, JIANG F, WEI D, LI H. Matt polyurethane coating: Correlation of surface roughness on measurement length and gloss [J]. *Polymers*, 2020, 12: 326.
- [41] HOLMBERG R J, BEAUCHEMIN D, JERKIEWICZ G. Characteristics of colored passive layers on titanium: Morphology, optical properties, and corrosion resistance [J]. *ACS Applied Materials and Interfaces*, 2014, 6: 21576–21584.
- [42] SUL Y T, JOHANSSON C B, PETRONIS S, KROZER A, JEONG Y, WENNERBERG A, ALBREKTSSON T. Characteristics of the surface oxides on turned and electrochemically oxidized pure titanium implants up to dielectric breakdown: The oxide thickness, micropore configurations, surface roughness, crystal structure and chemical composition [J]. *Biomaterials*, 2002, 23: 491–501.
- [43] BANDEIRA R M, RÊGO G C, PICONE C A, van DRUNEN J, CORRER W R, CASTELETTI L C, SPINOLA MACHADO A S, TREMILIOSI-FILHO G. Alternating current oxidation of Ti–6Al–4V alloy in oxalic acid for corrosion resistant surface finishing [J]. *SN Applied Sciences*, 2020, 2: 1092.
- [44] YANG C, DANG C Q, ZHU W L, JU B F. High-speed atomic force microscopy in ultra-precision surface machining and measurement: Challenges, solutions and opportunities [J]. *Surface Science and Technology*, 2023, 1: 7.
- [45] MALLAIAH M, GUPTA R K. Surface engineering of titanium using anodization and plasma treatment [J]. *IOP Conference Series: Materials Science and Engineering*, 2020, 943: 12016.
- [46] RADTKE A, EHLERT M, JĘDRZEJEWSKI T, SADOWSKA B, WIĘCKOWSKA-SZAKIEL M, HOLOPAINEN J, RITALA M, LESKELA M, BARTMANSKI M, SZKODO M,

- PISZCZEK P. Titania nanotubes/hydroxyapatite nanocomposites produced with the use of the atomic layer deposition technique: Estimation of bioactivity and nanomechanical properties [J]. *Nanomaterials*, 2019, 9: 123.
- [47] SHABANI M, ZAMIRI R. Effect of applied voltage and substrate preparation on surface modification of anodically oxidized titanium [J]. *Journal of Ovonic Research*, 2014, 10: 43–53.
- [48] MARZOUK R, SHOREIBAH E, MOTAWAE I, SHOEIB M. Preparation and characterization of $\text{TiO}_2\text{-SiO}_2$ bioceramic coating on Ti alloy via electrochemical anodization and its effect on corrosion resistance [J]. *Al-Azhar Dental Journal for Girls*, 2019, 6: 317–328.
- [49] HE D H, WANG P, LIU P, LIU X K, MA F, LI W, CHEN X H, ZHAO J, YE H. Preparation of hydroxyapatite-titanium dioxide coating on $\text{Ti}_6\text{Al}_4\text{V}$ substrates using hydrothermal-electrochemical method [J]. *Journal of Wuhan University of Technology: Materials Science Edition*, 2016, 31: 461–467.
- [50] MASAHASHI N, MORI Y, TANAKA H, KOGURE A, INOUE H, OHMURA K, KODAMA Y, NISHIJIMA M, ITOI E, HANADA S. Bioactive TiNbSn alloy prepared by anodization in sulfuric acid electrolytes [J]. *Materials Science and Engineering C*, 2019, 98: 753–763.
- [51] YAO C, WEBSTER T J. Anodization: A promising nanomodification technique of titanium implants for orthopedic applications [J]. *Journal of Nanoscience and Nanotechnology*, 2006, 6: 2682–2692.
- [52] KRČIL J, MÁRA V, KRUM S, SOBOTOVÁ J. The characterization of anodic oxide layers on selected biocompatible titanium alloys [J]. *Acta Polytechnica*, 2018, 58: 240–4.
- [53] KRČIL J, RAFAJ Z, MÁRA V, KRUM S, STARÝ V, NEHASIL V, SOBOTOVÁ J. The analysis of thermal and anodic oxide layers on selected biocompatible titanium alloys [J]. *Surface and Interface Analysis*, 2018, 50: 1007–1011.
- [54] ERAKOVIC S, JANKOVIC A, TSUI G C, TANG C Y, MISKOVIC-STANKOVIC V, STEVANOVIC T. Novel bioactive antimicrobial lignin containing coatings on titanium obtained by electrophoretic deposition [J]. *International Journal of Molecular Sciences*, 2014, 15: 12294–12322.
- [55] PAVLOVIĆ M R, ERAKOVIĆ S G, PAVLOVIĆ M M, STEVANOVIĆ J S, PANIĆ V V, IGNJATOVIĆ N L. Anaphoretical/oxidative approach to the in-situ synthesis of adherent hydroxyapatite/titanium oxide composite coatings on titanium [J]. *Surface and Coatings Technology*, 2019, 358: 688–694.
- [56] KODAIRA A, NONAMI T. Crystal structure and formation mechanism of spherical porous hydroxyapatite synthesised in simulated body fluid [J]. *Materials Technology*, 2019, 34: 185–191.
- [57] JAYASREE R, SAMPATH KUMAR T S. Acrylic cement formulations modified with calcium deficient apatite nanoparticles for orthopaedic applications [J]. *Journal of Composite Materials*, 2015, 49: 2921–2933.
- [58] LIU D M, TROCZYNSKI T, TSENG W J. Water-based sol-gel synthesis of hydroxyapatite: Process development [J]. *Biomaterials*, 2001, 22: 1721–1730.
- [59] KIM J H, KIM S H, KIM H K, AKAIKE T, KIM S C. Synthesis and characterization of hydroxyapatite crystals: A review study on the analytical methods [J]. *Journal of Biomedical Materials Research*, 2002, 62: 600–612.
- [60] JEONG J, KIM J H, SHIM J H, HWANG N S, HEO C Y. Bioactive calcium phosphate materials and applications in bone regeneration [J]. *Biomaterials Research*, 2019, 23: 1–11.

阳极氧化条件对骨整合用 α/β 钛合金表面沉积羟基磷灰石的影响： 原子力显微镜分析

Rania E. HAMMAM¹, Engie M. SAFWAT², Soha A. ABDEL-GAWAD³, Madiha SHOEIB⁴, Shimaa EL-HADAD⁴

1. Faculty of Engineering, Modern University for Technology and Information (MTI), Cairo 11585, Egypt;

2. Restorative and Dental Materials Department, National Research Centre, Giza 12622, Egypt;

3. Chemistry Department, Faculty of Science, Cairo University, Giza 12613, Egypt;

4 Central Metallurgical Research and Development Institute, CMRDI, P.O. 87, Helwan 11421, Egypt

摘 要：将钛基植入物与周围骨组织整合仍然具有挑战性。本研究旨在探讨不同阳极氧化电压(20~80 V)对双相(α/β)钛合金表面形貌的影响，并制备具有增强成骨能力的 TiO_2 薄膜。采用扫描电子显微镜结合能量色散光谱(SEM-EDS)和原子力显微镜(AFM) 研究合金的显微组织、化学成分和表面形貌，并确认其表面羟基磷灰石(HA)的生长。结果表明，与 Ti-6Al-4V 合金相比，Ti-6Al-7Nb 合金表面形成的 TiO_2 薄膜具有更优的粗糙度。在模拟体液中浸泡后，经 80 V 阳极处理的 Ti-6Al-7Nb 合金表面 HA 覆盖率提高，沉积的 HA 最多，其平均厚度为 $(128.38 \pm 18.13) \mu\text{m}$ 。结果表明经阳极氧化处理的钛合金具有良好的骨整合性及在人体内的稳定性，具有作为骨科植入材料的潜力。

关键词：材料科学；电化学阳极氧化；原子力显微镜； α/β 钛合金；羟基磷灰石沉积

(Edited by Wei-ping CHEN)